2011

The Influence of Pressure Relaxation on the Structure of an Axial Vortex

Robert L. Ash
Old Dominion University, rash@odu.edu

Irfan Zardadkhan
Old Dominion University

Allan J. Zuckerwar

Original Publication Citation

Ash, R. L., Zardadkhan, I., & Zuckerwar, A. J. (2011). The influence of pressure relaxation on the structure of an axial vortex. *Physics of Fluids, 23*(7), 073101. doi:10.1063/1.3609270

The influence of pressure relaxation on the structure of an axial vortex

Robert L. Ash,[1,a)] Irfan Zardadkhan,[1,b)] and Allan J. Zuckerwar[2,c)]
[1]*Department of Mechanical & Aerospace Engineering, Old Dominion University, Norfolk, Virginia 23529, USA*
[2]*NASA Langley Research Center, Mail Stop 238, Hampton, Virginia 23681, USA*

(Received 25 January 2011; accepted 26 May 2011; published online 26 July 2011)

Governing equations including the effects of pressure relaxation have been utilized to study an incompressible, steady-state viscous axial vortex with specified far-field circulation. When sound generation is attributed to a velocity gradient tensor-pressure gradient product, the modified conservation of momentum equations that result yield an exact solution for a steady, incompressible axial vortex. The vortex velocity profile has been shown to closely approximate experimental vortex measurements in air and water over a wide range of circulation-based Reynolds numbers. The influence of temperature and humidity on the pressure relaxation coefficient in air has been examined using theoretical and empirical approaches, and published axial vortex experiments have been employed to estimate the pressure relaxation coefficient in water. Non-equilibrium pressure gradient forces have been shown to balance the viscous stresses in the vortex core region, and the predicted pressure deficits that result from this non-equilibrium balance can be substantially larger than the pressure deficits predicted using a Bernoulli equation approach. Previously reported pressure deficit distributions for dust devils and tornados have been employed to validate the non-equilibrium pressure deficit predictions. © *2011 American Institute of Physics*. [doi:10.1063/1.3609270]

I. INTRODUCTION

The concept of "pressure relaxation" in fluids emerges naturally when the Navier-Stokes equations are derived utilizing variational principles. Most of the earlier variational formulations focused on inviscid fluids, but the variational method is also a powerful tool for introducing non-equilibrium effects in viscous fluids. Utilizing an approach similar to Serrin,[1] who employed Lagrange multipliers to incorporate conservation of mass, energy, and particle identity constraints in deriving the conservation of momentum equation for a compressible inviscid fluid, the present authors introduced dissipation in relaxing fluids previously by incorporating a "conservation of reacting species" constraint.[2] The addition of this constraint results in two volume-dissipative terms in the Navier-Stokes equation: first, the traditional "volume viscosity" term, proportional to the rate of dilatation, and second, a "pressure relaxation" term, proportional to the material time rate of change of the pressure gradient.[2,3] The appearance of two such terms is consistent with the requirement that a relaxation process be characterized by two independent constitutive coefficients.[4] Accordingly, the vector form of the resulting Navier-Stokes equation could be written as

$$\rho\frac{D\mathbf{v}}{Dt} = -\vec{\nabla}\left[P - \eta_p\frac{DP}{Dt}\right] - \rho\vec{\nabla}\Omega + \vec{\nabla}\left[\left(\eta_v - \frac{2}{3}\mu\right)\vec{\nabla}\cdot\mathbf{v}\right] + \vec{\nabla}\times\left(\mu\vec{\nabla}\times\mathbf{v}\right) + 2\left[\vec{\nabla}\cdot\left(\mu\vec{\nabla}\right)\right]\mathbf{v}, \quad (1)$$

where density, the total time derivative, velocity, and the gravitational potential, $\vec{\nabla}\Omega$, are in standard form, while η_P is the pressure relaxation coefficient (in seconds), η_V is the volume or bulk viscosity, and μ is the dynamic viscosity. If the pressure relaxation coefficient, volume viscosity, and dynamic viscosity are treated as constants, this conservation of momentum equation simplifies to

$$\rho\frac{D\mathbf{v}}{Dt} = -\vec{\nabla}P + \eta_P\vec{\nabla}\frac{DP}{Dt} - \rho\vec{\nabla}\Omega + \left(\eta_V + \frac{4}{3}\mu\right)\vec{\nabla}(\vec{\nabla}\cdot\mathbf{v}) - \mu\vec{\nabla}\times\left(\vec{\nabla}\times\mathbf{v}\right). \quad (2)$$

In the earlier work, the influence of volume-viscous and pressure relaxation effects on sound propagation, on the structure of a normal shock wave, and on Stokes flow around a sphere was investigated. The unexpected appearance of a constant-density, pressure-relaxation effect in a slow viscous Stokes flow has motivated the current examination of the influence of material rates of change of the pressure gradient, produced by streamline curvature, on the velocity and associated pressure distribution for a simple rotational flow.

Molecular dynamics simulations have demonstrated that non-equilibrium pressure (and temperature) can be manifest in constant density shear flows,[5,6] but the present work has explored its possible influence on large-scale incompressible continuum flows. The goal has been to investigate the structure of a steady incompressible axial vortex when the predicted pressure relaxation effects are included.

Tornadoes and dust devils (DD) resemble steady axial vortices for time intervals measured in minutes. Axial trailing line vortex signatures can also be observed to persist as condensation trails behind commercial aircraft at cruise altitudes, and the potential hazard that results when these trailing line vortices linger near congested airport flight paths is an important safety concern. Presently, computational fluid

[a)]Author to whom correspondence should be addressed. Electronic mail: Rash@odu.edu. Telephone: 757-683-4914. Fax: 757-683-3200.
[b)]Electronic mail: izard001@odu.edu.
[c)]Electronic mail: ajzuckerwar@yahoo.com.

dynamics models are unable to simulate the observed compact core behavior of these trailing line axial vortices.

Govindaraju and Saffman[7] examined the structure of turbulent trailing line vortices, observing that the initial axial velocity distribution resulting from the vortex generation process decayed long before the more persistent tangential (azimuthal) velocity distribution dissipated. They also pointed out that Lamb's diffusing unsteady laminar axial vortex model[8] neither predicts the instantaneous circulation distribution nor the experimentally observed circulation decay rates. Only two steady-state axial vortex velocity models are known and both are inviscid: the Rayleigh profile with a discontinuous radial velocity gradient and the potential vortex velocity profile with an infinite centerline velocity. Consequently, a theoretically based steady-state incompressible vortex model incorporating viscous core effects with an outer potential vortex structure can be of considerable use.

The modified Navier-Stokes equations have been used here to study an axial vortex with specified circulation. While the magnitude of a potential vortex velocity is unbounded for r $\rightarrow$ 0, potential vortices are employed to model a variety of important flows away from their viscous and turbulent origins. By assuming that these vortices derive from complex viscous interactions around physical bodies, a great deal of fluid mechanics literature has been focused on their far field behavior—predicting the behavior of trailing line vortex pairs behind moving objects is one example.[9] Obviously, potential flow models neglect vortex decay altogether while producing useful practical theory and justifying the development of quasi-steady vortex filament solutions that incorporate viscous and turbulent effects in their core or centerline regions. The steady-state solution that follows yields a velocity distribution that agrees with the most widely used empirical velocity profile model for aircraft trailing line vortices, while predicting that non-equilibrium pressure can play a decisive role in preserving the structure of these axial vortex structures.

II. EQUATIONS GOVERNING AN AXIAL VORTEX WITH PRESSURE RELAXATION

Neglecting body forces, Eq. (2) can be written as

$$\rho\frac{Dv_i}{Dt} = -\frac{\partial P}{\partial x_i} + \eta_p\frac{D}{Dt}\left(\frac{\partial P}{\partial x_i}\right) + \mu\frac{\partial^2 v_i}{\partial x_k^2} + \eta_p\left[\frac{\partial v_k}{\partial x_i}\frac{\partial P}{\partial x_k} - \frac{\left(\eta_v + \frac{1}{3}\mu\right)}{\eta_p}\frac{\partial}{\partial x_i}\left(\frac{1}{\rho}\frac{D\rho}{Dt}\right)\right]. \quad (3)$$

The term in braces was examined considering the possibility that pressure relaxation and volume viscosity could be linked to the production of sound in otherwise incompressible flows. Using the definitions from Zuckerwar and Ash,[2] $\eta_v = \rho_o a_o^2 \tau_{PS}$ and $\eta_p = \tau_{VS}$, where τ_{PS} is the constant-pressure relaxation time, τ_{VS} is the constant volume (density) relaxation time, ρ_o is the ambient density, and a_o is the ambient speed of sound, so that

$$\frac{\left(\eta_v + \frac{1}{3}\mu\right)}{\rho_o\eta_p} = a_o^2\frac{\tau_{PS}}{\tau_{VS}} + \frac{\nu}{3\tau_{VS}}. \quad (4)$$

In addition, the constant pressure and constant density relaxation times were related to each other through the high-frequency adiabatic compressibility, $\kappa_S^\infty = \frac{1}{\rho_o}\left(\frac{\partial\rho}{\partial P}\right)_{\xi,S}$, according to

$$a_o^2\frac{\tau_{PS}}{\tau_{VS}} = \frac{1}{\rho_o\kappa_S^\infty} = \frac{1}{\left(\frac{\partial\rho}{\partial P}\right)_{\xi,S}}, \quad (5)$$

where the subscripts for the partial derivative indicate constant entropy and constant progress variable. Consequently,

$$\frac{\eta_v + \frac{1}{3}\mu}{\eta_p} = \frac{\rho_o}{\left(\frac{\partial\rho}{\partial P}\right)_{\xi,S}} + \frac{\mu}{3\tau_{VS}}. \quad (6)$$

Using the data from Zuckerwar and Ash[2] for air and sea water, it was found that Eq. (6) could be approximated quite accurately (to three figures) using

$$\frac{\eta_v + \frac{1}{3}\mu}{\rho_o\,\eta_p} \approx\ a_o^2, \quad (7)$$

for those fluids. Therefore, at least for air and sea water, the term in braces in Eq. (3) can be modeled as

$$\begin{aligned}\eta_p\left[\frac{\partial v_k}{\partial x_i}\frac{\partial P}{\partial x_k} - \frac{\left(\eta_v + \frac{1}{3}\mu\right)}{\eta_p}\frac{\partial}{\partial x_i}\left(\frac{1}{\rho}\frac{D\rho}{Dt}\right)\right] &\approx \eta_p\left[\frac{\partial v_k}{\partial x_i}\frac{\partial P}{\partial x_k} - a_o^2\frac{\partial}{\partial x_i}\left(\frac{\rho_o}{\rho}\frac{D\rho}{Dt}\right)\right]\\ &\approx\ \eta_p\left[\frac{\partial v_k}{\partial x_i}\frac{\partial P}{\partial x_k} - a_o^2\frac{\partial}{\partial x_i}\left(\frac{D\rho}{Dt}\right)\right],\end{aligned} \quad (8)$$

for flows satisfying standard incompressibility constraints. The form of this last approximation suggests that it is a mechanism for sound production, where

$$\frac{\partial v_k}{\partial x_i}\frac{\partial P}{\partial x_k} = a_o^2\frac{\partial}{\partial x_i}\left(\frac{D\rho}{Dt}\right). \quad (9)$$

At any rate, it is assumed that when multiplied by the pressure relaxation coefficient, the contribution of Eq. (8) to the conservation of momentum equation is negligibly small for incompressible flows, and Eq. (3) can be simplified to

$$\rho\frac{Dv_i}{Dt} = -\frac{\partial P}{\partial x_i} + \eta_p\frac{D}{Dt}\left(\frac{\partial P}{\partial x_i}\right) + \mu\frac{\partial^2 v_i}{\partial x_k^2}. \quad (10)$$

A steady, incompressible, axial vortex has been examined, where the only velocity component is $v_\theta = v_\theta(r)$. For that case, the continuity equation is satisfied trivially, but the velocity and pressure distributions are coupled through the conservation of radial and azimuthal momentum equations. Neglecting body forces and using cylindrical coordinates, the material rate of change of the pressure gradient is the

only non-standard term in the incompressible governing Eq. (10). The three components of $\frac{D}{Dt}\vec{\nabla}P$, represented in cylindrical coordinates, are provided as an Appendix at the end of this article. In the present case, the radial component of the conservation of momentum equation, for $v_\theta = v_\theta(r)$, is unaffected by pressure relaxation and simplifies to

$$\rho\frac{v_\theta^2}{r} = \frac{dP}{dr}. \tag{11}$$

The azimuthal component of the conservation of momentum equation is not trivial due to the previously mentioned cross coupling between swirl velocity and radial pressure gradient via the material rate of change of the pressure gradient, thus requiring that the pressure relaxation forces balance with the viscous forces as follows:

$$0 = \eta_P\frac{v_\theta}{r}\frac{dP}{dr} + \mu\left[\frac{d^2v_\theta}{dr^2} + \frac{d}{dr}\left(\frac{v_\theta}{r}\right)\right]. \tag{12}$$

These two conservation of momentum equations can be combined to yield the following non-linear ordinary differential equation:

$$0 = \rho\eta_P\frac{v_\theta^3}{r^2} + \mu\left[\frac{d^2v_\theta}{dr^2} + \frac{d}{dr}\left(\frac{v_\theta}{r}\right)\right]. \tag{13}$$

For the case of an axial line vortex, the centerline velocity should be zero, while at large radii, the velocity should converge asymptotically to a prescribed circulation, Γ_o, i.e.,

$$\lim_{r\to\infty} v_\theta(r) \to \frac{\Gamma_o}{2\pi r}. \tag{14}$$

Employing kinematic viscosity, pressure relaxation coefficient, and circulation, dimensionless variables $\bar{r}$ and $u(\bar{r})$, defined by $r = \sqrt{\nu\eta_P}\,\bar{r}$ and $v_\theta = \frac{\Gamma_o}{2\pi\sqrt{\nu\eta_P}}u(\bar{r})$, can be employed in Eq. (13), along with a circulation-based Reynolds number $R_\Gamma = \frac{\Gamma_o}{2\pi\nu}$, to obtain the dimensionless governing equation,

$$\bar{r}^2\frac{d^2u}{d\bar{r}^2} + \bar{r}\frac{du}{d\bar{r}} - u(\bar{r}) + R_\Gamma^2u^3(\bar{r}) = 0, \tag{15}$$

subject to the boundary conditions

$$u(0) = 0, \tag{16}$$

$$\lim_{\bar{r}\to\infty}[\bar{r}u(\bar{r})] = 1. \tag{17}$$

The non-linear ordinary differential Equation (15) depends only on the boundary conditions and the Reynolds number. It should be noted that by utilizing an alternate dimensionless independent variable, ξ, and associated scaling parameter, k, given by

$$\xi = \sqrt{\frac{R_\Gamma^2-2}{2}}\ln\bar{r}, \qquad k = \sqrt{\frac{R_\Gamma^2}{2-R_\Gamma^2}} \qquad (R_\Gamma^2 \neq 2)$$

Eq. (15) transforms to

$$\frac{d^2u}{d\xi^2} = -\left(1+k^2\right)u + 2k^2u^3, \tag{18}$$

which is the standard differential equation governing Jacobi elliptic sn functions. However, the axial vortex boundary conditions are not completely compatible with that transformed independent variable.

III. STEADY-STATE SOLUTION FOR AN AXIAL LINE VORTEX

An alternate solution to Eq. (15) is given by

$$u(\bar{r}) + \sqrt{C_1^2 + u^2(\bar{r}) - \frac{R_\Gamma^2}{2}u^4(\bar{r})} = C_2\bar{r}, \tag{19}$$

and the zero centerline velocity requirement is satisfied when $C_1 = 0$. After imposing the far field boundary condition, the resulting dimensionless velocity profile can be written as

$$u(\bar{r}) = \frac{8\bar{r}}{8\bar{r}^2 + R_\Gamma^2}, \tag{20}$$

which is a surprisingly simple polynomial solution to the non-linear differential equation, depending only on the circulation-based Reynolds.

In order to compare the predicted velocity distribution with experimental measurements, it is convenient to revert to physical variables. Experimentally measured vortex core sizes have been defined in terms of the radius where the measured swirl velocity is a maximum. From Eq. (20), the corresponding maximum swirl velocity radius is given by

$$\frac{du}{d\bar{r}}(\bar{r}_{core}) = 0 \Rightarrow \bar{r}_{core} = \frac{R_\Gamma}{2^{3/2}} \Rightarrow r_{core} = \frac{R_\Gamma}{2^{3/2}}\sqrt{\nu\eta_p}. \tag{21}$$

Thus, the maximum core velocity can be written as

$$u_{\max}(\bar{r}_{core}) = \frac{\sqrt{2}}{R_\Gamma} \Rightarrow v_{\theta,\max} = \frac{1}{\sqrt{2\nu\eta_p}}\frac{\Gamma_o}{\pi R_\Gamma} = \sqrt{\frac{2\nu}{\eta_P}}. \tag{22}$$

It is useful to examine the influence of the pressure relaxation coefficient on the overall solution prior to comparison with the reported experimental measurements. The limiting cases of either very small or very large pressure relaxation coefficient can be examined most easily using the dimensional vortex core radius and maximum velocity expressions given by Eqs. (21) and (22), along with the dimensional velocity distribution representing Eq. (20),

$$v_\theta(r) = \frac{\Gamma_o}{\pi}\frac{2^{3/2}}{R_\Gamma\sqrt{\nu\eta_p}}\frac{(r/r_{core})}{(r/r_{core})^2+1}, \tag{23}$$

$$v_\theta(r) = 2\,v_{\theta,MAX}\,\frac{(r/r_{core})}{(r/r_{core})^2+1}. \tag{24}$$

When $\eta_p \to 0$, Eq. (21) shows that the limiting core radius approaches zero and from Eq. (22), the maximum core velocity approaches infinity, i.e., as the pressure relaxation coefficient vanishes, the exact solution approaches a potential vortex. For very large pressure relaxation coefficients, Eqs. (21) and (23) show that the velocity distribution evolves asymptotically toward a rigid-body rotation with an angular

rate of rotation approximated by $\Gamma_o/(\pi r_{core}^2)$ for $\eta_p \to \infty$. Hence, the present solution reverts to a potential vortex velocity profile when the pressure relaxation coefficient vanishes and to a rigid-body rotation when the pressure relaxation coefficient becomes very large.

From Eq. (21), it can be seen that the size of the vortex core varies linearly with circulation. Furthermore, for a given circulation, the physical magnitude of the vortex radius scales with $\sqrt{\nu\eta_P}$. From Eq. (22), the maximum swirl velocity does not depend on circulation, but instead is given by $\sqrt{(2\nu)/\eta_P}$. From these scaling relationships, it is observed that turbulent effects can be distinguished from the pressure relaxation effects, even when a simplified turbulent (eddy) viscosity model is employed. Pressure relaxation must be present in order for the present solution to exist, but it can be seen that increases in overall (effective) viscosity result in increases both in predicted core radius and maximum swirl velocity, whereas increases in the pressure relaxation coefficient result in increases in predicted vortex core radius, but the predicted maximum swirl velocity decreases. Nearly all of the axial vortex experiments cited in this work can be characterized as having turbulent cores. However, without detailed turbulence statistics, using measured maximum swirl velocity and core radius to estimate an appropriate eddy viscosity and the pressure relaxation coefficient is of limited utility. The actual fluid viscosity is an unambiguous minimum viscosity; therefore, using the fluid viscosity to correlate an effective pressure relaxation coefficient with a particular experimental measurement represents a limiting estimate.

Equation (24) is of the same functional form as the most widely used empirical fit for experimental aircraft trailing line vortex velocity profile data, proposed originally by Burnham and Hallock.[10] When the Burnham and Hallock model is adjusted so that the circulation at the vortex core radius is one-half the far field circulation, their experimental correlation is identical with Eq. (24). It should also be noted that Newman[11] employed an asymptotic analysis of a laminar vortex to model a quasi-steady vortex filament being convected downstream by a uniform axial velocity v_z and, thus, decaying with downstream distance z. Although Newman's solution was restricted to regions where $r/r_{core} \ll 1$, his asymptotic velocity profile expression was functionally the same as Eq. (23), differing only by the coefficient,

$$\frac{\Gamma_o}{4\pi}\sqrt{\frac{v_z}{\nu \cdot z}} \neq \frac{\Gamma_o}{\pi}\frac{2^{3/2}}{R_\Gamma\sqrt{\nu\eta_p}}.$$

Govindaraju and Saffman[7] pointed out that neither the Lamb diffusing laminar vortex model nor the Rayleigh vortex model predicts the correct circulation at the vortex core radius. While the experimental data they examined did not yield a precise circulation level at the core radius, they determined from those measurements that $\Gamma(r_{core})/\Gamma_o$ was between 0.4 and 0.6. The present authors are unaware of any recent circulation distribution data measured outside of ground effect that have improved our knowledge of the overall axial vortex circulation profiles behind moving vehicles. Wind tunnel and towing tank experiments cannot be employed to measure these circulation distributions because finite test section dimensions distort the velocity distributions. Since the theoretically predicted swirl velocity only varies with radius, the theoretical circulation distribution is given by the straight forward relation

$$\Gamma(r) = 2\pi \cdot r \cdot v_\theta(r) = 4\pi r \cdot v_{\theta,MAX} \cdot \frac{(r/r_{core})}{(r/r_{core})^2+1}, \quad (25)$$

$$\Gamma(r)/\Gamma_o = \frac{(r/r_{core})^2}{(r/r_{core})^2+1}, \quad (26)$$

which is plotted in Figure 1. In addition, it is important to recognize that the predicted circulation at the vortex core radius is given by

$$\Gamma(r_{core}) = \Gamma_o/2, \quad (27)$$

which is bracketed by the observations of Govindaraju and Saffman.[7] Hence, the present solution predicts that the vortex core circulation is equal to one-half the far field circulation, which is consistent with experiment over a significant range of circulation-based Reynolds numbers in air and water.

IV. VALIDATION OF THE PREDICTED VELOCITY PROFILE

Since the velocity distribution, given by Eq. (24), agrees with the empirical correlation most commonly employed to model the velocity distributions for aircraft trailing line vortices (with turbulent cores), it should be no surprise that the predicted velocity profile agrees with the experimental axial vortex velocity profile measurements reported in the literature over a wide range of circulation-based Reynolds numbers. As shown in Figure 2, the theoretical axial vortex velocity profile agrees with reported measurements for an aircraft flight experiment,[12] as well as for wind tunnel[13] and towing tank[14,15] experiments in air and water. At the larger vortex radii in water, the discrepancies between the present theory and the measurements of Baker *et al.*[15] are most probably due to the fact that those experiments were performed

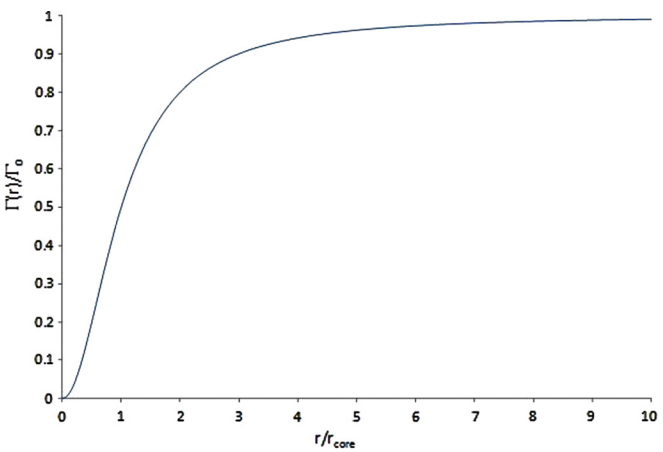

FIG. 1. (Color online) Variation of predicted circulation with radius, scaled with pressure relaxation parameter.

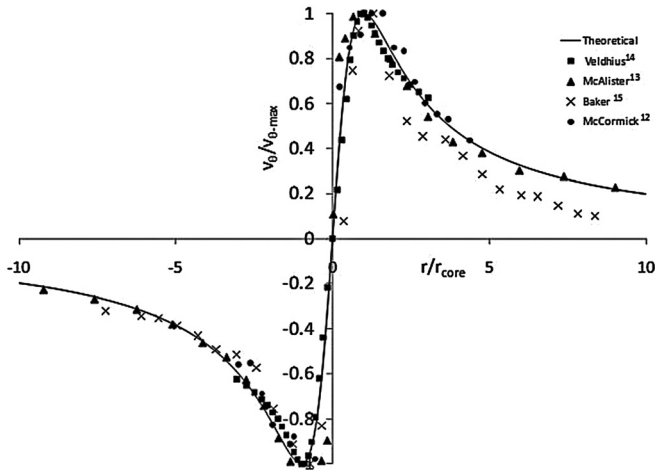

FIG. 2. Velocity distribution for a vortex filament with circulation Γ_o, scaled in terms of maximum velocity and its associated core radius.

in a towing tank where the finite tank dimensions distort the far field velocity distribution.

V. NON-EQUILIBRIUM PRESSURE VARIATION IN A CONSTANT DENSITY AXIAL VORTEX

The vortex velocity distribution, given by Eq. (16) or Eq. (17), is restricted to a constant density fluid. That restriction can be exploited by enabling Eq. (11) to be integrated directly to predict the vortex pressure distribution. Assuming that the far field pressure is P_∞, the pressure deficit produced by this vortex is given by

$$P_\infty - P(r) = \int_r^\infty \rho \frac{v_\theta^2(r)}{r} dr = \frac{4\mu R_\Gamma^2}{8\frac{r^2}{\nu} + \eta_p R_\Gamma^2} = 4\frac{\mu}{\eta_p} \frac{1}{\left(\frac{r}{r_{core}}\right)^2 + 1}. \tag{28}$$

From this relationship, the predicted centerline pressure deficit is given by

$$P_\infty - P(0) = 4\frac{\mu}{\eta_p} = 4\rho\frac{\nu}{\eta_P}, \tag{29}$$

which is twice the predicted pressure deficit associated with the (core) radius of maximum swirl velocity, and it is not controlled by the incompressible Bernoulli equation. In fact, the ratio of the pressure deficit predicted using the present model to the pressure deficit predicted by the incompressible Bernoulli equation is

$$\frac{2[P_\infty - P(r)]}{\rho \cdot v_\theta^2(r)} = 1 + \left(\frac{r_{core}}{r}\right)^2. \tag{30}$$

Since the centerline velocity is zero and the theoretically predicted centerline pressure deficit is a maximum, this result is not surprising. It is important to recognize that the pressure deficit is controlled by a balance between dynamic viscous forces and radial pressure gradient forces via the pressure relaxation coefficient. The incompressible Bernoulli equation predicts that the centerline pressure of an axial vortex (with a rigidly rotating core) returns to the far field pressure. In contrast, pressure relaxation predicts that the non-equilibrium pressure continues to decrease within the vortex core, reaching a minimum at the vortex centerline. When pressure relaxation effects are present, Eq. (29) shows that *smaller* pressure relaxation coefficients referenced to fluid viscosity produce *larger* departures from equilibrium, in order to balance the viscous forces. Alternatively, since an axial vortex core can be strongly turbulent in large-scale flows, at a given value of pressure relaxation coefficient, an increase in effective turbulent viscosity results in an increased pressure deficit.

Obviously, the larger pressure deficits, sustained by pressure relaxation, can play an important role in preserving compact laminar and turbulent axial vortex cores. Furthermore, the determination that either increased turbulent viscosity or decreases in pressure relaxation coefficient produce larger departures from equilibrium is reasonable because either smaller shear gradients associated with increased effective viscosity or larger material rates of change of the pressure gradient are needed to balance the forces. However, the constant density restriction employed in this analysis must necessarily break down for very small values of pressure relaxation coefficient and likewise for very large values of circulation. As will be shown, the pressure relaxation coefficients for air and water inferred from published axial vortex experiments can be very small.

VI. ESTIMATION OF THE PRESSURE RELAXATION COEFFICIENT FOR AIR AND WATER

The prevailing dissipative processes in air are: (1) vibrational relaxation of nitrogen, (2) vibrational relaxation of oxygen, and (3) rotational relaxation of nitrogen and oxygen, where the vibrational relaxation times of nitrogen and oxygen in air are known to be strong functions of humidity. Since the rotational collision numbers are estimated to be the same for nitrogen and oxygen, rotational relaxation is characterized by a single relaxation time. The translational (classical) relaxation times are too small to make a significant contribution and are, therefore, ignored.

The American National Standards Institute acoustical reference data[16] can be employed to estimate the pressure relaxation coefficient for air. Utilizing a mole-fraction-weighted averaging approach,[3] the influence of temperature and relative humidity (RH) on the estimated pressure relaxation coefficient is given in Table I. Following Herzfeld and Litovitz,[17] the relaxation times at low acoustical frequencies, corresponding to low Mach numbers, have been weighted by the relaxing specific heats.

For pure liquid water, there are two known dissipative processes: thermoviscous (classical) and structural. In the former, the thermal and viscous relaxation times under standard conditions are on the order of picoseconds. The structural process is based on transitions between an open ice-like molecular structure and a more close-packed structure. Measurements by Hall[18] indicate a relaxation time likewise on the order of a picosecond.

Alternatively, it is possible to use experimentally measured axial vortex velocity profiles to infer pressure relaxation

TABLE I. Acoustically based estimates of the pressure relaxation coefficient (in μs) for air at selected temperatures and relative humidities (Ref. 16).[a]

RH (%)	0	20	40	60	80	100
T, K						
273.15	43.38	2.58	1.31	0.88	0.66	0.53
283.15	50.52	1.78	0.91	0.61	0.46	0.37
293.15	58.23	1.28	0.64	0.43	0.32	0.26
303.15	66.50	0.93	0.47	0.31	0.23	0.18
313.15	75.31	0.69	0.34	0.23	0.17	0.13
323.15	84.64	0.52	0.26	0.17	0.12	0.10

[a]The pressure relaxation coefficient scales inversely with density, or for an ideal gas, with pressure. The reference pressure is 101 325 Pa (1 atm).

coefficients. In order to span the largest possible range of Reynolds numbers in air, the vortex velocity profile data for aircraft flight experiments and wind tunnel trailing line vortex experiments have been examined. Unfortunately, the actual atmospheric conditions, including humidity levels, were not reported consistently at flight altitudes for the trailing line vortex flight experiments, and thus, standard atmosphere tables were used to estimate kinematic viscosity when necessary. Wind tunnel test conditions were better-documented, but the influence of humidity was uncertain.

Delisi *et al.*[19] have summarized aircraft vortex core size measurements from 1995 and 1997 NASA flight experiments and from the 1990 National Oceanic and Atmospheric Administration (NOAA) flight test campaign conducted at Idaho Falls, Idaho. The NASA tests employed a Lockheed-Martin C-130 turboprop aircraft to generate trailing line vortices at 2000 m above ground level (outside of ground effect), and an instrumented OV-10 aircraft to probe the C-130 wake. Delisi *et al.*[19] reported on the smallest and largest encountered C-130 trailing line vortex cores, but they did not report the temperature and humidity—thus, a nominal or average vortex core for the C-130 has been used in the table that follows. On the other hand, Garodz and Clawson[20] used a suite of meteorological instruments in association with the 1990 NOAA fly-by tests using Boeing 757 and 767 aircraft, enabling influences of ambient temperature and relative humidity on the pressure relaxation coefficient to be examined. The NOAA test campaign report summarizes 241 tower fly-by data sets, including Boeing 727 aircraft flights, but for the purposes of establishing the utility of incorporating the pressure relaxation coefficient in trailing line vortex velocity models, only the extreme cases for the two primary Boeing aircraft have been examined herein. In addition to the NASA wake encounter tests and the NOAA large commercial airplane tests in the ground effect, McCormick, Tangler, and Sherrier[12] measured the vortex core velocity profiles behind a Piper Cherokee out of ground effect. The pressure relaxation coefficients were calculated from the experimental velocity profile data using estimated initial circulation, based on aircraft weight and flight speed, and the measured core radii. From Eq. (21), the pressure relaxation coefficient can be estimated as

$$\eta_p = 2\nu\left(\frac{4\pi \cdot r_{core}}{\Gamma_o}\right)^2 = \left(\frac{4\pi \cdot r_{core}}{\Gamma_o}\right)^2 \frac{2\mu}{\rho}, \tag{31}$$

where, in the absence of a prescribed effective turbulent viscosity, the dynamic viscosity of the fluid has been used. The quadratic dependence on the ratio of the measured core radius and the theoretically based circulation (neglecting decay) most certainly influences the accuracy of these estimates. For the representative wind tunnel tests, the imposed circulation was not readily estimated, but the vortex core radius and maximum swirl velocity were measured more accurately than for flight tests. In those experiments, the circulation, Γ_o, was assumed to be $\Gamma_o = 4\pi r_{core} v_\theta(r_{core})$, and the measured maximum swirl velocity was employed to estimate the far field circulation. Since the actual circulation levels and ambient conditions are somewhat uncertain, and the theory-based pressure relaxation coefficients, given in Table I, have not yet been validated experimentally, it is not advisable to separate turbulent viscosity effects from the pressure relaxation effects using these data. Hence, the experimental velocity profiles have been correlated with the theory using an effective pressure relaxation coefficient as the only adjusted parameter and the calculated effective pressure relaxation coefficients are summarized in Table II.

The use of a turbulent eddy viscosity, varying linearly with circulation, was first proposed by Squire[22] as an approach for modeling the decay of trailing line vortices. While that type of isotropic turbulence model is of limited utility in the vicinity of the vortex generator,[23] recent experiments have shown that downstream axial vortex core radius growth and maximum swirl velocity decay can be scaled using turbulent eddy viscosity.[24] Pending experimental validation of the theoretically based pressure relaxation coefficients, a turbulent viscosity adjustment for the steady-state axial vortex solution should be used with extreme caution.

The NOAA vortex measurements were made using a downwind 60.96 m (200 ft) tower, instrumented at 0.610 m (2 ft) intervals, during the fly-bys. Thus, the Garodz and Clawson NOAA flight tests[20] were the only data where the predicted sensitivity of the pressure relaxation coefficient to atmospheric conditions could be examined. Since those flight experiments utilized an instrumented tower, the trailing line vortices were influenced both by ground effects and by vortex age (due to the time delay between the aircraft crossing the plane of the instrumented tower and the arrival of the generated vortices). The four tests included in Table II were for the largest measured maximum core rotational velocity and for the smallest measured maximum core rotational velocity for the Boeing 757 and for the Boeing 767 tests, with no adjustments for ground effects or vortex filament age. The ambient conditions corresponding to the actual vortex crossing are given beneath the experiment entries in the table. For comparison, the pressure relaxation coefficients using the recorded atmospheric conditions in Table I are given in italics beneath the vortex-derived pressure relaxation coefficient estimates. Using the recorded flight speed V, aircraft weight W, and wing span b, as provided in the NOAA data report,[20] the far field circulation was estimated assuming elliptically loaded wings. Thus, the initial circulation for each flight was estimated using

$$\Gamma_o = \frac{4}{\pi}\frac{W}{\rho_\infty V b}, \tag{32}$$

TABLE II. Estimates of pressure relaxation coefficients in air based on vortex experiments.[a]

Experiment	Γ_o (m^2/s)	R_Γ	r_{core} (m)	ν (m^2/s)	η_p (μs)
NASA C-130 (Ref. 19)	200	2 100 000	0.34	15.1×10^{-6}	0.0134
NOAA B-757 (Ref. 20)	40.55 (16 s)	380 500	0.061	16.96×10^{-6}	0.0121
9 °C; 74% RH					(*0.53*)
NOAA B-757 (Ref. 20)	35.41 (35 s)	330 200	0.274	17.07×10^{-6}	0.323
10.5 °C; 52% RH					(*0.72*)
NOAA B-767 (Ref. 20)	37.46 (59 s)	356 800	0.091	16.71×10^{-6}	0.0311
7.0 °C; 51% RH					(*0.84*)
NOAA B-767 (Ref. 20)	43.53 (25 s)	381 500	0.244	18.16×10^{-6}	0.180
21 °C; 18% RH					(*7.0*)
Piper Cherokee (Ref. 12)	10.2	105 000	0.046	15.4×10^{-6}	0.0990
McAlister and Takahashi (Ref. 13)	8, 5	81 600, 51 000	0.02, 0.03	15.6×10^{-6}, 15.6×10^{-6}	0.0308, 0.177
Graham (Ref. 21)	2.2	23 200	0.009	15.2×10^{-6}	0.0803

[a]The time interval between aircraft crossing the plane of the instrumented tower and vortex arrival is given in parentheses after the estimated circulation in Goradz and Clawson (Ref. 20). Pressure relaxation coefficient corresponding the recorded temperature and humidity, using Table I, is given in parentheses under the vortex-based estimate.

where ρ_∞ is the ambient air density. In that way, the measured core radius was the only experimentally measured quantity employed directly in the estimates of pressure relaxation coefficient. The order of magnitude difference between the estimated pressure relaxation coefficient for the large-core B 757 vortex and the small-core B 767 vortex does not appear to be consistent with a 3.5 °C change in ambient temperature and likely represents sensitivity to vortex core turbulence and experimental error in estimating the pressure coefficient.

From Eq. (22), the maximum vortex velocity is given by $\sqrt{\frac{2\nu}{\eta_p}}$, and the pressure relaxation coefficient estimates from Table II can be used to compare the predicted maximum velocities with the measured maximum velocities for the four (extreme case) tower fly by tests. The comparison of the predicted maximum core velocities, using the unadjusted elliptically loaded wing circulation estimates, along with the predicted maximum pressure deficit at the center of these vortices (Eq. (29)) are summarized in Table III. As before, an effective pressure relaxation coefficient has been used as the only adjustable parameter.

Had the measured maximum vortex core velocity and measured core radius been employed simultaneously to adjust the instantaneous far-field circulation for the NOAA data, the predicted maximum velocities using Eq. (22) agreed with the measured velocities to within a standard deviation of 7.1%, but some of the estimated far field circulation levels, calculated by assuming that the vortex core circulation was one-half the far-field circulation, were higher than the estimated initial circulation for an elliptically loaded wing (undoubtedly due to wind shear and ground effects). In either case, the theoretically predicted pressure deficits are substantially larger than the maximum dynamic pressures associated with the maximum rotational velocities, but measured vortex pressure deficits were not tabulated.

Pressure relaxation coefficients for water can be estimated from towing tank experiments. Water experiments generally have smaller velocity uncertainty intervals than for large-scale experiments in air, and while the circulation-based Reynolds numbers for the tabulated water experiments are rather low, the measured profiles likely were influenced by turbulent core effects. It is more difficult to estimate the far field circulation; furthermore, the finite width and depth of the experimental facilities distort the vortex trajectories and associated velocity distributions. For the data contained in Table IV, the far field circulation was assumed to be equal to twice the circulation calculated at the vortex core radius. These data suggest that the effective pressure relaxation coefficient for water is on the order of 50 μs, approximately 100 times larger than the pressure relaxation coefficients for air and substantially larger than the picosecond molecular relaxation times associated with water.

To summarize, the pressure relaxation coefficient estimates for air using acoustical reference data and mole-weighted averages, given in Table I, require experimental

TABLE III. Comparison of predicted and measured maximum vortex velocities using the Garodz and Clawson (Ref. 20) data along with predicted core pressure deficits.

Experiment	T (°C)	Mole fraction Water Vapor	Theory $\sqrt{\frac{2\nu}{\eta_p}}$ (m/s)	Measured (m)/s	$P_\infty - P(0) = 4\frac{\mu}{\eta_p}$ (kPa)
NOAA B-757 (Ref. 20)	9	0.01016	52.9	99.4	5.8
9 °C; 74% RH					
NOAA B-757 (Ref. 20)	10.5	0.00785	10.3	7.3	0.22
10.5 °C; 52% RH					
NOAA B-767 (Ref. 20)	7.0	0.00612	32.8	57.8	2.25
7.0 °C; 51% RH					
NOAA B-767 (Ref. 20)	21	0.00531	14.2	7.4	0.40
21 °C; 18% RH					

TABLE IV. Estimation of pressure relaxation coefficients in water based on experiment.

Experiment	Γ_o (m^2/s)	R_Γ	r_{core} (m)	ν (m^2/s)	η_p (s)
De Gregorio and Ragni (Ref. 25)	0.101	1.658×10^4	0.0180	9.79×10^{-7}	9.8×10^{-6}
Veldhuis *et al*. (Ref. 14)	0.0428	6.958×10^3	0.0180	9.79×10^{-7}	54.7×10^{-6}
Baker *et al*. (Ref. 15)	0.0155	2.467×10^3	0.0076	1×10^{-6}	75.9×10^{-6}
Shekarriz *et al*. (Ref. 26)	0.0149	2.610×10^3	0.0088	9.1×10^{-7}	100×10^{-6}

verification because the actual circulation, ground effect, and wind shear corrections, along with an effective turbulent viscosity, cannot be deduced from the four NOAA tower-flyby tests where ambient temperature and humidity were recorded. The pressure relaxation coefficients for pure water cannot be estimated accurately using acoustical data, but the magnitudes of the characteristic molecular relaxation times imply pressure relaxation coefficients that are substantially smaller than those that correlate the experimental vortex core radii and velocities measurements.

VII. VALIDATION OF NON-EQUILIBRIUM PRESSURE DEFICIT PREDICTIONS

Pitot tubes, including five-hole and seven-hole vortex probes, have been commonly used to measure vortex velocity distributions. Since the present theory predicts that the difference between local stagnation and static pressure within an axial vortex core is not equal to the dynamic pressure, pitot probe data cannot be used directly to isolate non-equilibrium pressure deficits. Hot film and hot wire anemometer measurements of velocity should be more accurate, but it is difficult to measure the associated local static pressure and velocity simultaneously because of probe interference. A more desirable laboratory approach could utilize particle imaging velocimetry to measure vortex velocities in the vicinity of the vortex core, in concert with a miniature static pressure survey probe. Obviously, large-diameter axial vortex experiments are preferred because the non-equilibrium pressure departures can be resolved more accurately in the core region since the pressure deficit varies more slowly with distance in large-diameter vortices, but accompanying turbulence contributions must be measured simultaneously.

Sinclair[27] used an instrumented mobile 9.14 m (30 ft) tower to measure dust devil vortex properties on flat desert terrain, near Tucson, AZ. Dust devils, like water spouts, have similar features to tornadoes, with vortex lifetimes approaching 4 min, but without the complications resulting from atmospheric moisture transport processes. During a typical dust devil event, it is possible to forecast the likely vortex track with sufficient accuracy to position an instrumented mobile tower directly on the expected path. That was the approach utilized by Sinclair. His mobile tower incorporated custom-built heated thermocouple anemometers to measure instantaneous wind speeds, resistance thermometers to measure ambient temperatures and custom-built, and fast-response capacitive pressure transducers to measure instantaneous static pressures at three tower heights. Temperature, pressure deficit, rotational velocity, and axial velocity distributions were measured for three dust devils in August, 1962. Ambient temperatures varied between 42.5° and 47°C, during the dust devil encounters, and even though the relative humidity and ambient pressure were not recorded, the nominal desert elevation was 780 m, while the average summertime midday dew point temperature in nearby Tucson is 8 °C. Hence, the relative humidity (near 10%) could be estimated using the nominal dew point temperature and the pressure relaxation coefficient could be gotten from Table I. The estimated pressure relaxation coefficients for the three dust devil encounters varied between 1.009×10^{-6} and 1.125×10^{-6} s. Sinclair's data were recorded cinematically and he reported dust devil diameters for dust devils designated DD#1, DD#2, and DD#3, and maximum pressure deficits for dust devils DD#1 and DD#2. The maximum core velocities could be gotten from his graphical data, and at 2.1 m (7 ft) above ground level, the maximum core velocities were 11, 12, and 8.8 m/s for DD#1, DD#2, and DD#3, respectively. Thus, the corresponding estimated far field circulation levels were 318, 392, and 370 m^2/s. Unlike the aircraft wake, tow tank, and wind tunnel measurements, Sinclair measured dust devil diameters, along with velocity, pressure deficit, and temperature distributions for the three dust devils. Consequently, even though his data were less accurate than more modern measurement systems, the dust devil measurements provide an opportunity to differentiate effective turbulent viscosity effects from pressure relaxation coefficient effects.

Using the predicted pressure relaxation coefficients from Table I, the coefficient values corresponding to the three dust devil cases only varied by approximately ±6%. The maximum pressure deficit predicted from Eq. (29), and Sinclair's data can be used to estimate an effective turbulent viscosity (eddy viscosity added to kinematic viscosity) for each dust devil. Subsequently, the effective turbulent viscosity and the theoretically based pressure relaxation coefficient can be used in Eq. (22) to predict the maximum swirl velocity. By comparing the predicted maximum core velocities with the experimentally measured maximum velocities, the pressure deficit predictions can be validated indirectly. Those data are tabulated in Table V, where it can be seen that the effective turbulent viscosities are reasonably consistent and the predicted maximum velocities agree with the measured maximum velocities to within a standard deviation of ±17%. Although this is a large standard deviation, a comparison between the theoretically predicted pressure deficit and velocity distributions and Sinclair's measurements for a representative Dust devil measurement set (DD#2), as shown in Figure 3, suggests that the theory and data are consistent. Obviously, the turbulent effects are present and the measured data are quite noisy, but Sinclair's reported maximum pressure deficits are consistent with more recent dust devil data.[28]

TABLE V. Estimated effective turbulent viscosity and comparison between predicted maximum and measured maximum core velocities for Sinclair (Ref. 27) dust devils.

Dust devil	r_{core} (m)	Γ_o (m^2/s)	RH (%)	η_P (μs)	$-\Delta P_{max}$ (mb)	ν_{eff} (m^2/s)	v_{theory} (m/s)	v_{max} (m/s)
#1	2.3	318	13	1.049	2.86	7.1×10^{-5}	11.8	11
#2	2.6	392	10	1.125	2.53	7.1×10^{-5}	11.2	12
#3	3.35	370	11	1.092	2.30	6.2×10^{-5}	10.7	8.8

The theoretical axial vortex solution can also be used in a simplified, vortex-filament tornado model to examine measured tornado core pressure deficits. Recently, Karstens *et al.*[29] have summarized near-ground pressure and wind speed measurements from instrumented tornado encounters. Utilizing hardened *in situ* pressure probes and mobile mesonet instrumentation, they reported that nine tornadoes have been probed successfully. Those tornadoes exhibited pressure deficits ranging from 5 hPa to 194 hPa, although the extreme case (21 April 2007, Tulia, TX tornado[30]) was measured using a mobile vehicle that was overrun by the tornado. Karstens *et al.*[29] and others have discounted the extreme pressure deficit data taken in the F-4 Tulia tornado because the pressure instrumentation could not be adjusted or calibrated to account for the rather violent event that occurred when the vehicle was within the tornado core. The extreme pressure deficit could be discounted on that basis and also because they estimated that the wind speeds for the Tulia tornado would have been 135 m/s (Mach number ≈ 0.4), even when they used an adjusted pressure deficit of 170 hPa rather than the reported deficit[30] of 194 hPa. In their view, the second-largest pressure deficit (95 hPa, measured during the 24 June 2003 Manchester, SD tornado) had a more realistic estimated maximum wind speed of 95 m/s.

Highly resolved numerical models for tornadoes involve three-dimensional unsteady processes, including thermal convection and multi-phase transport of water.[31,32] Furthermore, if the associated vortex wind speeds exceed 100 m/s, it is difficult to justify the constant density restriction for the present steady-state solution. However, if the cyclonic core pressures are controlled by pressure relaxation, it is useful to examine the pressure data compiled by Karstens *et al.*,[29] particularly with regard to the extreme pressure deficit measured in the Tulia, TX tornado. Karstens *et al.*[29] used time series to construct pressure deficit profiles, centered with respect to the rotational axes of the tornadoes. Five data sets associated with four tornadoes (7 May 2002, Mullinville, KS; 24 June 2003, Manchester, SD, two data sets; 11 June 2004, Webb, IA; and 29 May 2008, Tipton, KS) had pressure versus radius plots (Figure 7 in their article) that were sufficiently symmetric to permit the estimation of core size. Tornado cores are highly turbulent and the ratio of effective viscosity to pressure relaxation coefficient is the basic correlation parameter from Eq. (29), i.e.,

$$\frac{\nu_{turb}}{\eta_P} = \frac{P_\infty - P(0)}{4\rho}. \tag{33}$$

If no adjustment is made for turbulence, the dynamic viscosity of air depends only on temperature, and the effective pressure relaxation coefficient can be estimated as follows:

$$\eta_P = \frac{4\mu}{P_\infty - P(0)}. \tag{34}$$

From Eq. (22), the maximum core velocity depends only on the ratio of the viscosity to the pressure relaxation coefficient. Hence, using Eq. (33) it is not necessary to distinguish turbulent effects and pressure relaxation effects, and the maximum measured pressure deficit can be used to estimate the maximum tornado core velocity directly,

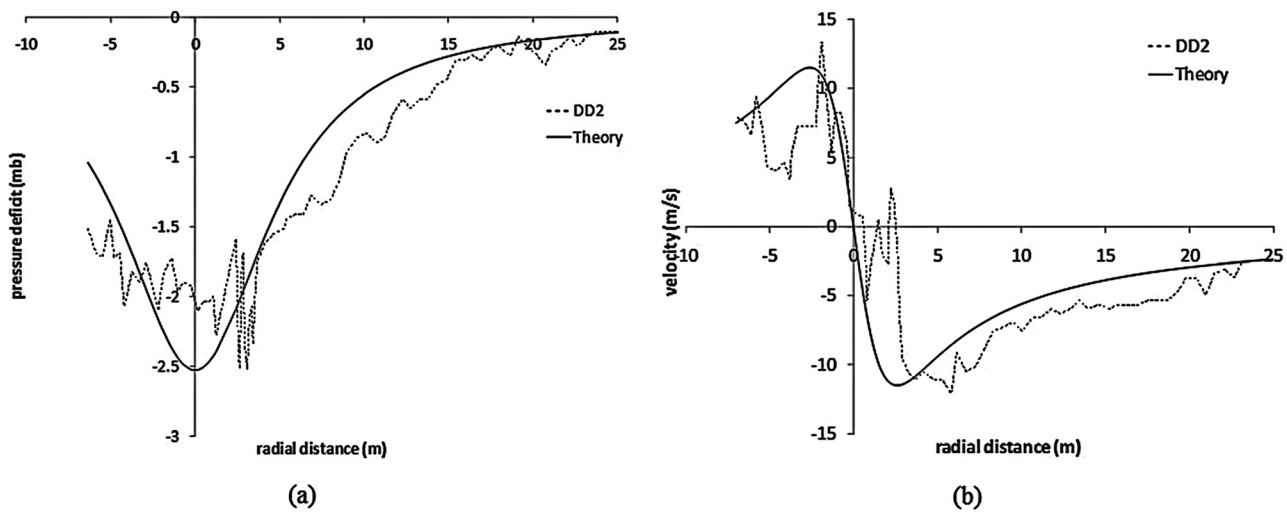

FIG. 3. Comparison between measured and predicted (a) pressure deficit variations for Sinclair (Ref. 27) Dust Devil #2 and (b) velocity profiles for Sinclair (Ref. 27) Dust Devil #2.

TABLE VI. Estimation of pressure relaxation coefficient and corresponding maximum wind speed for recent tornadoes, using measured pressure deficit and associated core radius.

Tornado	$\lvert\Delta P\rvert_{Max}$ (hPa)	η_P (μs)	R_{core} (m)	Maximum velocity (m/s)	Γ_o (m^2/s)
7 May 2002 (Ref. 29) Mullinville, KS	22	0.033	265	32.4	108 000
24 June 2003 (Ref. 29) Manchester, SD	98	0.008	36	68.4	31 000
24 June 2003 (Ref. 29) Manchester, SD	55	0.013	15	51.2	9 600
11 June 2004 (Ref. 29) Webb, IA	27	0.027	54	35.8	24 200
29 May 2008 (Ref. 29) Tipton, KS	15	0.048	205	26.8	69 000
21 April 2007 (Ref. 30) Tulia, TX	194	0.004	30	96.1	36 200

$$v_{\theta,MAX} = v_\theta(r_{core}) = \sqrt{\frac{1}{\rho}\left[\frac{P_\infty - P(0)}{2}\right]}. \tag{35}$$

Tornado core radii can be estimated from the pressure distribution plots in Karstens *et al.*[29] using the relation

$$\frac{P_\infty - P(r_{core})}{P_\infty - P(0)} = \frac{1}{2}. \tag{36}$$

Finally, the core radius and associated velocity can be used to estimate the circulation,

$$\Gamma_\infty = 2[2\pi\, r_{core} v_{\theta,MAX}]. \tag{37}$$

The requisite tornado data for the selected tornadoes are tabulated in Table VI. In addition, the experimentally measured pressure distributions associated with those tornadoes, as plotted by Karstens *et al.*,[29] but normalized with respect to each maximum pressure deficit and its associated core radius are compared with the theoretical pressure distribution (Eq. (28)) in Figure 4(a). Figure 4(b) is an image of an emerging tornado spout whose shape is similar to the theoretical pressure distribution. The effective pressure relaxation coefficients estimated using the tornado pressure data are in the same range as the estimated pressure relaxation coefficients inferred from the aircraft wake and wind tunnel axial velocity measurements in Table II, although the estimated circulation levels are three orders of magnitude larger. From Table VI, the pressure deficit measured in the Tulia, TX tornado yields a realistic maximum swirl velocity when pressure relaxation effects are included. Furthermore, the damage sustained by the chase vehicle[30] that briefly penetrated the tornado core appears to be consistent with a sudden exposure to a 346 kph (215 mph) wind. Clearly, the pressure distribution predicted by Eq. (28) is in very good agreement with the normalized time-series plots of the four symmetric tornado pressure profiles in Karstens *et al.*[29] Furthermore, the pressure deficits measured during the other tornado events suggest that the associated maximum velocities are rather low, possibly because the deployed pressure probes were not directly beneath the actual tornado centers of rotation. If the other tornado pressure deficits were associated with the tornado core boundary pressure rather than the centerline pressure minimum, the estimated maximum wind speeds should be increased by the square root of two.

VIII. CONCLUSIONS

Inclusion of pressure relaxation effects can represent a controlling factor in sustaining axial vortex structures. The velocity profile predicted by this theory is essentially identical with the empirical Burnham and Hallock[10] correlation

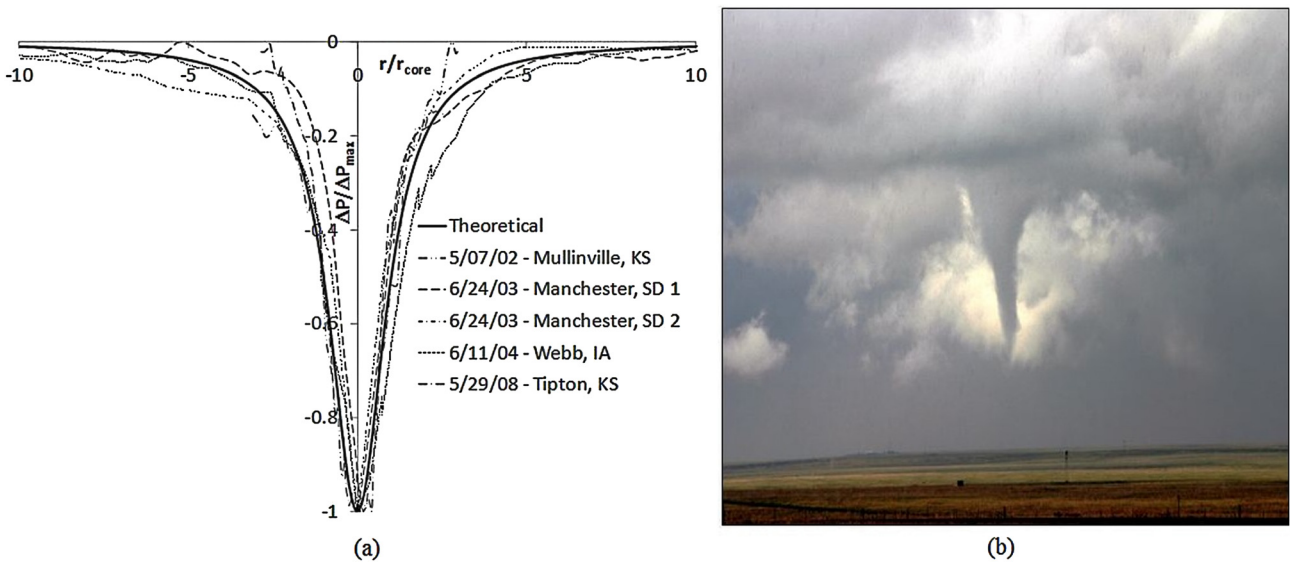

FIG. 4. (Color online) (a) Comparison of normalized tornado pressure deficit distributions from Karstens *et al.* (Ref. 29) with $-\left[\left(\frac{r}{r_{core}}\right)^2 + 1\right]^{-1}$, the normalized pressure distribution predicted from Eq. (28). (b) Image of an emerging tornado spout, showing the similarity between its visible cloud boundary and the predicted pressure deficit distribution.

for aircraft wake velocity profiles when the predicted relationship between vortex core radius, viscosity and pressure relaxation coefficient is introduced. Furthermore, the estimates of the effective pressure relaxation coefficients for air and water, using previous vortex experiments, have been shown to be reasonably consistent over circulation-based Reynolds numbers ranging from 23 000 in a wind tunnel experiment to 5×10^8 for a tornado and over approximately two orders of Reynolds number magnitude in water. An effective turbulent viscosity can be justified in the vicinity of the vortex core and that adjustment produces similar modifications to the predicted velocity and pressure distributions as a decrease in the pressure relaxation coefficient. The theoretically based pressure relaxation coefficient for the dry atmospheric conditions associated with three dust devil encounters[27] produced reasonably consistent estimated turbulent viscosities when the theoretically predicted pressure relaxation coefficients were employed. In agreement with theory,[3] the influence of humidity on pressure relaxation coefficient appears to be significant, as inferred from aircraft wake velocity profile and tornado pressure deficit profile measurements. However, without accounting for turbulence using an effective or eddy viscosity, the pressure relaxation coefficients inferred from the experimental data are not in good agreement with the theoretically based mole-weighted humid air estimates, warranting further investigation. Since the pressure relaxation coefficients inferred from tornado pressure deficit data are similar to those inferred from aircraft wake vortex and wind tunnel experiments, an eddy viscosity correction may be sufficient, but the aircraft and tornado data do not support Squire's[22] proposed linear dependence of eddy viscosity on circulation.

The present theoretical pressure relaxation coefficient-based velocity and pressure distributions were used as a simplified tornado model in order to estimate the maximum core velocity associated with the "excessive" 194 hPa pressure deficit recorded in the Tulia, TX, F-4 tornado.[30] Using that recorded pressure deficit, the estimated maximum core velocity was consistent with F-4 tornado velocities, suggesting that many of the other reported tornado pressure deficit profiles[29] may not have probed the vortex core centers.

Pressure relaxation coefficients for liquid water could only be inferred utilizing the experimental vortex velocity profile measurements because existing acoustical data were too scattered to support a consistent theory. However, the experimentally inferred pressure relaxation coefficients were several orders of magnitude larger than relaxation times associated with the known dissipative processes in water. Since strong vortices in liquid water can cause the core region to cavitate, whereas the strong vortices in humid air can produce water condensation boundaries (similar to the emerging tornado condensation boundary shown in Figure 4(b)), it is possible that non-equilibrium two-phase processes involving water should be included in a more comprehensive theoretical model for estimating pressure relaxation coefficients for those fluids. The consistency between the shapes of the predicted velocity and pressure profiles and experimental measurements over a wide range of turbulent conditions suggests that an effective turbulent viscosity can be used that also contributes to possible pressure relaxation coefficient corrections. Controlled axial vortex experiments, measuring turbulence effects and isolating the various pressure relaxation processes would be very useful.

The fact that pressure relaxation produces a simple exact solution for an important axial flow, while predicting simultaneously that non-equilibrium pressures within the cores of these rotating flows are much lower than predicted by equilibrium dynamic pressure estimates is an appealing result, since it can explain why vortex filaments can be sustained in simple fluids for extended periods of time without dilating as rapidly as predicted by conventional Navier-Stokes models.

ACKNOWLEDGMENT

The authors would like to thank Dr. Joseph A. Werne of NorthWest Research Associates for motivating an examination of the basic modeling assumptions employed in the original manuscript and the referees for their helpful comments and suggestions.

APPENDIX: NON-STANDARD MATERIAL RATE OF CHANGE OF PRESSURE GRADIENT COMPONENTS

In cylindrical coordinates, the three components of the material rate of change of the pressure gradient, $\frac{D}{Dt}\vec{\nabla}P$, can be represented as follows, where the radial, azimuthal, and axial velocities are v_r, v_θ, and v_z, respectively:

Radial component:

$$\frac{\partial^2 P}{\partial t \partial r} + v_r \frac{\partial^2 P}{\partial r^2} + \frac{v_\theta}{r}\frac{\partial^2 P}{\partial \theta\, \partial r} + v_z \frac{\partial^2 P}{\partial z \partial r} - \frac{v_\theta}{r^2}\left(\frac{\partial P}{\partial \theta}\right).$$

Azimuthal component:

$$\frac{1}{r}\frac{\partial^2 P}{\partial t \partial \theta} + \frac{v_r}{r}\frac{\partial^2 P}{\partial r \partial \theta} + \frac{v_\theta}{r^2}\frac{\partial^2 P}{\partial \theta^2} + \frac{v_z}{r}\frac{\partial^2 P}{\partial z \partial \theta} + \frac{v_\theta}{r}\left(\frac{\partial P}{\partial r}\right) - \frac{v_r}{r^2}\left(\frac{\partial P}{\partial \theta}\right).$$

Axial component:

$$\frac{\partial^2 P}{\partial t \partial z} + v_r \frac{\partial^2 P}{\partial r \partial z} + \frac{v_\theta}{r}\frac{\partial^2 P}{\partial \theta\, \partial z} + v_z \frac{\partial^2 P}{\partial z^2}.$$

[1] J. Serrin, "Mathematical principles of classical fluid mechanics," in *Handbuch Der Physik*, edited by S. Flugge (Springer-Verlag, Berlin, 1959), Vol. VIII/1, pp. 144–150.
[2] A. J. Zuckerwar and R. L. Ash, "Variational approach to the volume viscosity of fluids," Phys. Fluids **18**, 047101 (2006).
[3] A. J. Zuckerwar and R. L. Ash, "Volume viscosity in fluids with multiple dissipative processes," Phys. Fluids **21**, 033105 (2009).
[4] J. Meixner, "Allgemeine Theorie der Schallabsorption in Gasen und Flussigkeiten unter Berucksichtigung der Transporterscheinungen," Acustica **2**, 101 (1952).
[5] D. J. Evans and G. P. Morriss, *Statistical Mechanics of Non-Equilibrium Liquids*, 2nd ed. (Cambridge University Press, Cambridge, England, 2008), pp. 297–300.
[6] J. Casas-Vázquez and D. Jou, "Temperature in non-equilibrium states: A review of open problems and current proposals," Rep. Prog. Phys. **66**, 1937 (2003).

[7]S. P. Govindaraju and P. G. Saffman, "Flow in a turbulent trailing vortex," Phys. Fluids **14**(10), 2074 (1971).
[8]H. Lamb, *Hydrodynamics*, 6th ed. (Dover, New York, 1945), pp. 591–592.
[9]I. Lakkis and A. Ghoniem, "A high resolution spatially adaptive vortex method for separating flows. Part I. Two-dimensional domains," J. Comput. Phys. **228**, 491 (2009).
[10]D. C. Burnham and J. N. Hallock, "Chicago monostatic acoustic vortex sensing system. Volume IV, Wake vortex decay," National Technical Information Service, Alexandria VA, Report No. DOT/FAA/RD-79-103, Volume 4, 1982.
[11]B. G. Newman, "Flow in a viscous trailing vortex," *Aeronautical Quarterly*, Vol. 10, pp. 149–162 (May 1959).
[12]B. W. McCormick, J. L. Tangler, and H. E. Sherrier, "Structure of trailing vortices," J. Aircr. **5**, 260 (1968).
[13]K. W. McAlister and R. K. Takahashi, "NACA 0015 Wing pressure and trailing vortex measurements," NASA Technical Paper No. 3151 and AVSCOM Technical Report No. 91-A-003, 1991.
[14]L. L. M. Veldhuis, F. Scarano, and C. Van Wijk, "Vortex wake investigation of an Airbus A340 model using PIV in a towing tank," Proceedings of the 21st AIAA Applied Aerodynamics Conference, Orlando, FL, AIAA Paper No. 2003-3814, June 2003.
[15]G. R. Baker, S. J. Barker, K. K. Bofah, and P. G. Saffman, "Laser anemometer measurements of trailing vortices in water," J. Fluid Mech. **65**, 325 (1974).
[16]ANSI Standard S1.26-1995, "Method for calculation of the absorption of sound by the atmosphere" (Standards Secretariat of the Acoustical Society of America, New York, 1995).
[17]K. F. Herzfeld and T. A. Litovitz, *Absorption and Dispersion of Ultrasonic Waves* (Academic, New York, 1959), See Eqs. (21-18).
[18]L. Hall, "The origin of ultrasonic absorption in water," Phys. Rev. **73**, 775 (1948).
[19]D. P. Delisi, G. C. Greene, R. E. Robins, D. C. Vicroy, and F. Y. Wang, "Aircraft wake vortex core size measurements," Proceedings of the 21st AIAA Applied Aerodynamics Conference, Orlando, FL, AIAA Paper No. 2003-3811, June 2003.
[20]L. J. Garodz and K. L. Clawson, "Vortex wake characteristics of B757-200 and B767-200 aircraft using the tower fly-by technique," NOAA Technical Memorandum ERL ARL 199, 1993.
[21]W. R. Graham, "Experimental assessment of the extended Betz method for wake vortex prediction," Proceedings of the AGARD 78th Fluid Dynamics Panel Meeting and Symposium, Trondheim, Norway, Paper T-9, May 1996.
[22]H. B. Squire, "The growth of a vortex in turbulent flow," Aeronaut. Q. **16**, 302 (1965).
[23]J. S. Chow, G. G. Zilliac, and P. Bradshaw, "Mean and turbulence measurements in the near-field of a wingtip vortex," AIAA J. **35**(10), 1561 (1997).
[24]S. C. C. Bailey and S. Tavoularis, "Measurement of the velocity field of a wing-tip vortex, wandering in grid turbulence," J. Fluid Mech. **601**, 281 (2008).
[25]F. De Gregorio and A. Ragni, "Wake vortex characterisation in towing tank facilities using PIV technique," Proceedings of the 41st Aerospace Sciences Meeting and Exhibit, Reno, NV, AIAA Paper No. 2003-93, January 2003.
[26]A. Shekarriz, T. C. Fu, and J. Katz, "Near-field behavior of a tip vortex", AIAA J. **31**, 112 (1993).
[27]P. C. Sinclair, "The lower structure of dust devils," J. Atmos. Sci. **30**, 1599 (1969).
[28]M. Balme and R. Greeley, "Dust devils on Earth and Mars," Rev. Geophys. **44**, RG3003, doi: 10.1029/2005RG000188, (2006).
[29]C. D. Karstens, T. M. Samaras, B. D. Lee, W. A. Gallus, Jr., and C. A. Finley, "Near-ground pressure and wind measurements in tornadoes," Mon. Weather Rev. **138**, 2570 (2010).
[30]S. F. Blair, D. R. Deroche, and A. E. Pietrycha, "In situ observations of the 21 April 2007 Tulia, Texas tornado," Electronic J Severe Storms Meteor. **3**(3), 1 (2008).
[31]D. C. Lewellen and R. I. Sykes, "Large-eddy simulation of a tornado's interaction with the surface", J. Atmos. Sci. **54**, 581 (1997).
[32]D. C. Lewellen and W. S. Lewellen, "Near-surface intensification of tornado vortices", J. Atmos. Sci. **64**, 2176 (2007).